Enriched mantle generated through persistent convective erosion of continental roots

T. M. Gernon[a,b,*], S. Brune[b,c], T. K. Hincks[a], M. R. Palmer[a], C. J. Spencer[d], E. J. Watts[a,e], A. Glerum[b]

[a] *School of Ocean & Earth Science, University of Southampton, Southampton SO14 3ZH, UK*
[b] *GFZ Helmholtz Centre for Geosciences, Potsdam, Germany*
[c] *University of Potsdam, Potsdam-Golm, Germany*
[d] *Department of Geological Sciences & Geological Engineering, Queen's University, Kingston, Canada*
[e] *Now at: Department of Geography, Faculty of Science and Engineering, Swansea University, Swansea, UK*

The origin of geochemically enriched mantle in the asthenosphere is important to understanding the physical, thermal, and chemical evolution of Earth's interior. While subduction of oceanic sediments and deep mantle plumes have been implicated in this enrichment, they cannot fully explain the observed geochemical trends. Here we use geodynamic models to show that enriched mantle can be liberated from the roots of the sub-continental lithospheric mantle by highly organised convective erosion, a process tied to continental rifting and breakup. We demonstrate that this 'chain' of convective instabilities sweeps enriched lithospheric material into the sub-oceanic asthenosphere, in a predictable and quantifiable manner, over tens of millions of years—potentially faster for denser, removed keels. We test this model using geochemical data from the Indian Ocean Seamount Province, a near-continent site of enriched volcanism with minimal deep mantle plume influence. This region shows a peak in enriched mantle volcanism within 50 million years of breakup followed by a steady decline in enrichment, consistent with model predictions. We propose that persistent and long-distance lateral transport of locally metasomatised, removed keel can explain the billion-year-old enrichments in seamounts and ocean island volcanoes located off fragmented continents. Continental breakup causes a reorganisation of shallow mantle dynamics that persists long after rifting, disturbing the geosphere and deep carbon cycle.

Enriched mantle (EM) components are parts of Earth's mantle that contain distinct concentrations of certain trace elements relative to the average or depleted mantle (DM)[1]. EM components, an enduring feature of the asthenosphere frequently detected in ocean island basalts (OIBs), give rise to heterogeneous radiogenic isotope compositions in mantle domains[1,2]. While compositionally diverse at all scales[3,4,5], the 'Enriched Mantle 1' (EM1) end-member is typically characterised by higher $^{87}Sr/^{86}Sr$ ratios, lower $^{143}Nd/^{144}Nd$, and generally lower $^{206}Pb/^{204}Pb$ ratios when compared to DM[1,2,6]. EM1-type enrichment is frequently associated with continental margins, such as the Walvis Ridge off the coast of Africa in the Atlantic Ocean[7] (Extended Data Fig. 1), and the Indian Ocean Seamount Province, originally off north-eastern Australia[8]. What is lacking are mechanistic models that show how this enrichment, particularly prominent in the earliest volcanism at such sites[7,8], may occur. We propose that organised chains of Rayleigh-Taylor instabilities, which sweep along continental keels following breakup[9,10], can systematically disturb ancient deep lithospheric reservoirs, flushing the removed enriched components into the sub-oceanic asthenosphere over tens of millions of years (Myr).

Various sources have been proposed for EM1's origins, including subducted oceanic crust with pelagic sediments[2]; deeply subducted lower continental crust[11]; deep-rooted mantle plumes that mobilise subducted material[12]; and recycled sub-continental lithospheric mantle (SCLM)[4,13,8]. Notably, the EM1 group of OIBs share common features, yet each occurrence exhibits diverse trends that extrapolate to a variety of Pb isotope ratios at high Sr and low Nd isotope ratios[14]. This suggests that EM1 was not generated from a homogeneous source during a single event: it taps a mosaic of rocks of varying ages.

The mantle reservoirs feeding OIBs likely remained chemically isolated for 1–2 billion years (Gyr), allowing isotopic systems (e.g., U/Pb, Sm/Nd) to evolve after shallow (that is, upper mantle or crustal) fractionation[15]. Chemical isolation can occur within the lowermost SCLM, where EM1-type enrichment can occur through metasomatic fluids driven off subducting slabs[16] (Fig. 1). Geophysical and geochemical constraints[17,18] suggest these fluids ascend and impregnate the SCLM keel[4,19] and accumulate in multiple stages over several Gyr[20,21,22], isolating them from convective mantle. During continental breakup, enriched SCLM domains become entrained into the sub-oceanic asthenosphere[8,17,18], though the duration and length-scales of this process remain uncertain. Such enriched domains can contain carbonate and hydrous phases, lowering the solidus temperature during decompression melting, fuelling OIB volcanism[21].

The mechanisms for entraining lowermost SCLM into the asthenosphere during continental breakup include thermal erosion and lateral advection directly under the rift zone[18,23]. Conti-

*Corresponding author: T.M.Gernon@soton.ac.uk

nental breakup drives lithospheric thinning, giving rise to upwelling and possibly decompression melting involving laterally flowing cratonic material[23]. Such processes are generally thought to be restricted to the immediate post-rift phase. The persistence of EM1 signatures in volcanic rocks erupted many tens of Myr after local breakup[24,25] and the presence of these signatures within contiguous chains or areas of volcanism over similar periods[12,17] implies an enduring supply of EM1-type material that is not well explained by existing models.

We investigate the possibility that EM1-type domains are supplied to the shallow asthenosphere from the SCLM through the far-field effects of rifting[9,10]. Active rifting and necking—the pronounced thinning of the lithosphere as plates separate—creates lithospheric edges, introducing lateral temperature and viscosity gradients. These gradients generate edge-driven convection (EDC) cells within the underlying mantle[26,27], which both mechanically disturb the adjacent continental root[9], and deflect local mantle upwellings[28]. Indeed, cool 'hotspots' in the oceans may either have a shallow source or result from deep plume material being cooled and redistributed by small-scale convection[29,30,28]. Further, some oceanic intraplate lavas have been linked to small-scale sub-lithospheric convective instabilities associated with upwelling induced by buoyant decompression melting[31]. In addition to organising small-scale convection near the rift, EDC can instigate a chain of Rayleigh-Taylor instabilities that systematically migrate continent-ward along the lithospheric root[9,10]. Whilst this process destabilises the metasomatised continental keel, driving low-degree melting, devolatisation, and kimberlite volcanism[9], much of the removed keel is entrained into the asthenosphere where it either sinks or migrates ocean-ward. Crucially, destabilisation of the keel can continue tens of Myr after continental breakup, reflecting the time taken for instabilities to migrate into craton-interiors[9,10]. Therefore, lithospheric contamination of asthenospheric mantle may be much more protracted than previously envisaged.

Characterising EM1-Type Volcanism

To evaluate whether convective removal of lithospheric keels could influence magma petrogenesis in the oceanic realm, we first studied the geochemical characteristics of kimberlites and adjacent contemporaneous oceanic volcanism. Kimberlites, which erupted extensively across the cratons during Gondwana breakup[32], provide a window into the geochemical evolution of the deep SCLM they sample[9]. To examine the relationship between SCLM and EM1, we consider a compilation of kimberlite radiometric ages and geochemical data from Southern Africa including ϵNd_i[33] and $(^{87}Sr/^{86}Sr)_i$[34] (Figs. 2a–c; Extended Data Fig. 1). Earlier kimberlites are more enriched and show both EM1 and subduction zone signatures, with varying degrees of crustal contamination (Figs. 2a–c). Kimberlite compositions then abruptly become depleted, with Sr and Nd isotope trends toward DM end-members[35] (Fig. 2a), suggesting a greater influence of SCLM assimilation earlier in kimberlite petrogenesis, followed by stronger input of asthenospheric mantle (Figs. 2b–c). This evolution implicates SCLM delamination and adiabatic upwelling of asthenosphere[9]. Notably, delamination thins the lithosphere and can drive continental exhumation[10,21,36].

The mantle flow beneath Africa is driven by a large-scale upwelling that diverges beneath the continent, causing westward mantle movement beneath the South Atlantic continental margins of Africa[36]. This prevailing mantle flow, generated above the deeper Couette (shear) flow, should transport decoupled SCLM into the Atlantic asthenosphere[36]. Lithospheric delamination on this scale should be discernible in oceanic basalts near the continent-ocean boundary (COB). To investigate this, we examine geochronological and isotopic data from volcanic rocks on Walvis Ridge[7,37] (Figs. 2d–f) near the Congo and Kaapvaal cratons (Extended Data Fig. 1). The earliest Walvis volcanism at 114 Ma[7] followed accelerated rifting and breakup (Figs. 2d–e)[38], intense exhumation along adjacent margins (Extended Data Fig. 2), and delamination of the distant Kaapvaal craton[9] (Figs. 2b–c). Walvis volcanics lag the Etendeka plume volcanism (Extended Data Fig. 1) by ~20 Myr and exhibit enriched compositions—followed by an abrupt transition to more depleted compositions—mirroring the kimberlite trend (Fig. 2). To investigate the timing, we apply a conjugate partitioned recursion—a computational approach that can identify change-points in time series (Methods)—finding that the Walvis volcanics indeed show a similar shift to depleted compositions, albeit ~7 Myr later (Figs. 2d–e). Accordingly, we suggest that the early phases of Walvis volcanism primarily reflect SCLM removal during South Atlantic rifting and breakup, potentially influenced by interaction with residual mantle upwellings[28] that aided breakup[12,39].

The question remains, however, whether the dynamics of convective removal can allow for the transport of SCLM to the sub-oceanic asthenosphere on timescales required by the changing geochemical signatures (Fig. 2).

Geodynamic Modelling of Rifting and Breakup

We address this question by utilising thermo-mechanical simulations (building on refs.[9,10]) to quantify the magnitude and rate at which enriched material is removed from keels and delivered to the sub-oceanic asthenosphere (Methods). Previous simulations show that Rayleigh-Taylor instabilities initiate at the lithospheric discontinuity and migrate toward the continent, stripping weak, metasomatised keels[9,10]. While we focus on simulations that best match observations from kimberlites[9] and exhumation patterns[10], we used additional experiments to assess the effects of varying lithospheric thickness, two-way plate motion, alternative mantle rheologies (including variations in viscosity of the asthenosphere and metasomatised mantle lithosphere[9]), and a deeper model domain (Methods). The process of sequential delamination occurs in all scenarios as described in the reference model (Fig. 3a). Migration rates of instabilities differ slightly from the reference model (Fig. 3), but are in full agreement with observational constraints[9,10] (Methods).

We observe that a large component of the removed keel is entrained into convection cells and transported ocean-ward (Fig. 3a). To estimate the flux of SCLM into the sub-oceanic asthenosphere, we quantify the total amount of this material be-

low the lithospheric discontinuity in the model domain at 0.5 Myr intervals (Methods). In the reference model, SCLM enters the sub-oceanic asthenosphere within ~2 Myr of breakup, defined as the point when the continental lithosphere within the rift is fully separated[38]. Its abundance peaks within 15–50 Myr post-breakup and declines over time, reflecting the progressive removal and exhaustion of lithospheric keels by convective erosion (Figs. 3a–b). To test the sensitivity of this result, we vary the extension velocity (5 mm yr^{-1} and 20 mm yr^{-1}, compared with 10 mm yr^{-1} in the reference model) and introduce symmetric boundary conditions (Methods; Supplementary Videos 1–5). These changes shift the timing of SCLM flux peaks but, except in slow-extension cases (Extended Data Fig. 3), do not change the overall pattern: peaks consistently occur within ~50 Myr of breakup and broadly decline over time (Fig. 3b). Faster divergence rates, which are common during the rift-drift transition[38], lead to an accelerated 'mantle wind' and more vigorous convection (Supplementary Video 3), transporting detached SCLM more rapidly into the oceanic asthenosphere (Fig. 3b). In contrast, under slow extension, where rifting is protracted (lasting ~140 Myr), the main peak occurs during late-stage rifting (Extended Data Fig. 3). Such cases are not relevant to the scenarios discussed below and are not considered further. Expanding the model domain depth to 410 km has little effect on the spacing (thus, wavelength) of instabilities, which decreases slightly from 270 km to 255 km (Methods).

In all models, we observe clear spikes—periods lasting several Myr—when decoupled SCLM enters the sub-oceanic asthenosphere at high flow rates (Fig. 3b). To detect whether these pulses are cyclic, we apply a Lomb-Scargle periodogram—an algorithm used to identify periodic signals in unevenly sampled data[40] (Methods)—finding that pulses exhibit a statistically significant periodicity (p-value < 0.05) of 5–6 Myr (Extended Data Fig. 4). While the SCLM flux does not directly correspond to EM1, the EM1 field closely overlaps with xenoliths and volcanics representing the lowermost SCLM[41,42] (Fig. 2a). We therefore assume that EM1 scales with the SCLM tracer in our models. Crucially, our model does not require all this SCLM to melt to generate volcanism: it simply predicts where and when candidate EM1 reservoirs were present during, and viably stimulated, melting.

To further test the operating limits of our mechanism, we conducted 27 numerical experiments varying the density and viscosity of the metasomatised lithospheric keel, while holding all other parameters constant. The results reveal three broad behavioural regimes (Extended Data Fig. 5). For intermediate densities (3290–3310 kg/m^3; 0.3–0.9% above ambient SCLM), the system evolves comparably to the reference case (Fig. 3). At higher densities (≥3320 kg/m^3), dripping has concluded by 50 Myr post-rift onset, with detached keel pockets entrained in small-scale convection (Extended Data Fig. 5). Here, rapid flushing of removed material and shorter residence times imply that associated EM-type magmatism would peak during or soon after rifting. At lower densities (≤3280 kg/m^3), buoyancy inhibits dripping, instead favouring lateral flow of metasomatised material towards the rift (Extended Data Fig. 5), akin to the underplating of ref.[23]. These findings accord with theoretical predictions: migration rates increase with density and decrease with increasing viscosity (higher activation energies)[9]. These experiments define a viable parameter space for the proposed mechanism (Extended Data Fig. 5), most of which result in transport of removed SCLM into the sub-oceanic asthenosphere.

This removed material is entrained into convection cells, tied to lithospheric edge effects (Fig. 3a), which may superpose on the expected 5–6 Myr periodicity. This raises the question of the timescale required for EM signals to manifest in oceanic volcanism. To explore this, we consider a range of indicative length scales (350–500 km) and maximum velocities taken from geodynamic simulations for a Monte Carlo analysis of convection cells (Extended Data Fig. 6; Methods). This yields a first-order estimate of the time lags, with median and mean ascent times of ~8 and ~9 Myr, respectively (Figs. 3c–d).

These results allow us to make testable predictions. First, enriched SCLM should enter the sub-oceanic asthenosphere within a few Myr of breakup (Fig. 3b; Supplementary Videos 1–5), but then requires 5–15 Myr to reach the surface (Figs. 3c–d). Second, the supply of enriched material should persist for tens of Myr, gradually declining over time, with peak supply occurring within ~50 Myr of breakup (Fig. 3b), potentially sooner in cases where higher-density keels delaminate (Extended Data Fig. 5). Third, the transfer rate of enriched material to the surface should be pulsed, reflecting episodic delamination operating on six-million-year cycles (Fig. 3b), modulated by mantle convection on eight-million-year cycles (Figs. 3c–d). While such periodicity could be detected in the tempo of oceanic volcanism, there are currently insufficient data to rigorously test this.

Testing Convective Erosion Models for the EM Signal

To test the first two predictions, we examine ocean crust and seamount provinces that are not associated with HIMU mantle plume signatures to avoid the complication of volcanism sampling deep mantle sources. This setting is best exemplified by the Indian Ocean, where mid-ocean ridge basalt (MORB) exhibits more enriched compositions than those of the Pacific and North Atlantic[41,43]. This enrichment has been linked to shallow recycling of continental material, including the SCLM and lower crust[8,44,45,46,47,48]. Specifically, we investigate the Christmas Island Seamount Province (CHRISP) in the eastern Indian Ocean (Fig. 4)—far from known deep mantle plume influence[30]—where EM1-enriched end-members were identified in the SCLM of NW Australia[8]. We include the nearby Investigator Fracture Zone[41] (Fig. 4b), where early-stage enrichment from delaminated SCLM during Gondwana breakup is thought to have declined over time through mixing with depleted upper mantle[41].

We compile radiometric ages and isotopic characteristics of volcanic rocks spanning the IFZ[41] and the CHRISP (Fig. 5a; Supplementary Table 1), where they are typically 0–25 Myr younger than the underlying oceanic crust[8]. We applied a weighted bootstrap analysis to mitigate the effect of spatial sampling bias (Methods). We identify an early peak in EM1 involvement in melting within 40–60 Myr of the final

breakup of India from Antarctica–Australia, which occurred ~126 Ma[38,49] (Fig. 5a). The earliest post-breakup volcanism occurred ~116 Ma (10 Myr post-breakup), closely consistent with model predictions (Fig. 3c). Volcanics closer to Australia exhibit greater enrichment, suggesting a predominantly Australian SCLM source, as proposed by Hoernle et al.[8]. Indeed, the occurrence of kimberlite volcanism in western Australia at 120 Ma[32] may indicate disruption of the SCLM keel then[9]. The isotopic trajectory of volcanics trends towards West Australian lamproites[8] and the proposed EM1 end-member of ref.[42], while some data trend towards African kimberlites and the EM1 end-member of ref.[41] (Fig. 5a). Variable Pb isotope signatures likely reflect age heterogeneity in the SCLM, sourced from different continental regions with varying storage durations. We infer a long-term decline in the contribution of enriched material to melting, reflected, for example, in a steady increase in $(^{206}Pb/^{204}Pb)_i$ over time ($r^2 = 0.71$; Fig. 5b), similar to other isotope systems (e.g., Extended Data Fig. 7). These trends mirror the long-term decline in enrichment in our geodynamic models (Fig. 3b).

We observe similar trends at other classic EM sites (albeit where cold/warm plumes are present[30]), namely the Kerguelen Plateau (EM2 end-member), Broken Ridge, and Ninetyeast Ridge in the Indian Ocean, which once formed a contiguous province (Extended Data Fig. 8a; Supplementary Tables 1–3). The early phases of EM-type magmatism in these regions are broadly similar to the IFZ/CHRISP regions (Fig. 5): enriched signatures peak within 50–60 Myr of breakup, superimposed on a long-term decline, as reflected in a steady increase in $(^{206}Pb/^{204}Pb)_i$ over time ($r^2 = 0.57$, n = 181; Extended Data Fig. 8b). Notably, extreme EM1 signals in the Afanasy-Nikitin Rise seamounts (~600 km from Broken Ridge) has been linked to shallow recycled continental lithosphere[44], consistent with the episodic 'spikes' of enrichment predicted by our model (Fig. 3b).

Global Implications

Taken together, our data and observations support a model in which convective removal of SCLM supplies enriched material to the sub-oceanic asthenosphere, explaining both the early peak and long-term decline[41] in enriched components involved in mantle melting (Fig. 5a–b). We infer that this decline reflects a progressive reduction in the volume of delaminated SCLM entering the sub-oceanic asthenosphere (Fig. 3). This laterally propagating cratonic material reaches shallow mantle depths when the oceanic lithosphere is young and thin[50]. The upwelling EM1-bearing mantle undergoes decompressional melting while simultaneously metasomatising the nascent oceanic lithosphere[50].

This highly organised convective erosion of lithospheric keels (Fig. 3) is a global physical process that creates a diffuse 'pool' of ancient lithospheric domains in the upper mantle. This material, shaped by the complex and long-term (i.e., Gyr) thermochemical[51] and metasomatic[52] evolution of the lithospheric roots, most closely resembles the composition of the putative EM1 mantle end-member (Figs. 2a, 5a). This heterogeneous material radiated outward from the cratonic roots during and after Gondwana breakup (Fig. 4a; Extended Data Fig. 1). This mechanism may thus provide insights into the origin and distribution of the extensive DUPAL isotope anomaly, which is linked to the EM1 reservoir[1,43,53] and shows a geospatial association with Gondwana breakup zones[54] (Fig. 4a; Extended Data Fig. 1). Indeed, geochemical evidence from deep xenoliths indicate that the SCLM carries DUPAL isotope characteristics[55], consistent with suggestions that DUPAL is a shallow mantle feature[20,56]. Rather than remaining stagnant since Gondwana breakup[54], DUPAL's present-day distribution[53] (Extended Data Fig. 1) may reflect a persistent flow of decoupled, highly heterogeneous SCLM from the continental roots into the sub-oceanic asthenosphere, perhaps reconciling the geochemical similarity between OIBs and some continental intraplate basalts[57].

Our geodynamic models indicate that convective erosion of lithospheric keels can persist long after continental breakup, exerting a waning influence over time (Fig. 3b), punctuated by transient pulses of enrichment that extend even to distant parts of the oceanic plate. These findings support the view that the EM1 source taps an ancient, enriched SCLM reservoir[20,21]. The same 'mantle wave-like' mechanism—previously invoked to explain kimberlite volcanism[9] and plateau uplift[10] in cratonic settings—operates on predictable timescales, which are manifested in major seamount provinces (Figs. 2, 4, 5; Extended Data Figs. 7–8). This offers a viable, perhaps auxiliary, alternative to deep-mantle plumes in explaining Gyr-old enrichments in ocean island volcanism associated with fragmented continental margins. Given the prevalence of hydrous and carbonated phases in the SCLM[9,18,20,21], this process may have exerted a dominant influence on the volatile supply to oceanic volcanoes through time, with implications for the geosphere and the deep carbon cycle.

Acknowledgements

T.G. and T.H. gratefully acknowledge funding from the WoodNext Foundation, a donor-advised fund program. S.B. is funded by the European Research Council (ERC) (EMERGE; award number: 101087245). We thank the Computational Infrastructure for Geodynamics (geodynamics.org) which is funded by the National Science Foundation under award EAR-0949446 and EAR- 1550901 for supporting the development of ASPECT. The authors gratefully acknowledge the computing time granted by the Resource Allocation Board and provided on the supercomputer Lise at NHR@ZIB as part of the NHR infrastructure. The calculations for this research were conducted with computing resources under the project bbp00039. The maps shown in Fig. 4a and Extended Data Fig. 8a were plotted with the open source plate tectonic application software GPlates (https://www.gplates.org/), which is licensed for distribution under a GNU General Public License, and the open source spatial mapping software QGIS (https://qgis.org/). In Fig. 4, the the underlying bathymetric data were obtained from GeoMapApp v. 3.7.4 (https://www.geomapapp.org/), which incorporates topographic relief from the Global Multi-Resolution

Topography (GMRT) synthesis. For the purpose of open access, the author has applied a CC BY public copyright licence to any Author Accepted Manuscript version arising from this submission.

Author Contributions

Conceptualisation and project administration: T.G.; Conceptualisation of geodynamic models: S.B., A.G.; Methodology, formal analysis, and software: T.H., T.G., E.J.W. (R), S.B., A.G. (ASPECT, Paraview), C.J.S. (CPR); Investigation: T.H., T.G., E.J.W., S.B., A.G., C.J.S., M.R.P.; Funding acquisition: T.G.; Visualisation: T.H., S.B., A.G., T.G.; Writing – original draft: T.G. Writing – review and editing: all authors.

Competing interests

The authors declare no competing interests.

Figure Captions

Figure 1: Generation of enriched mantle (EM) under the continents. EM components accumulate over Gyr timescales through multiple phases of enrichment. This can occur through the upwelling (that is, return flow) of carbon-bearing melts from the mantle transition zone, as well as the percolative upward transport of carbonated melts sourced from down-going subducted oceanic slabs. This process metasomatises the cratonic keels, resulting in spatially heterogeneous age profiles and EM compositions. Diamond symbols denote regions where diamonds are thought to accumulate. TBL: thermal boundary layer; MORB: mid-ocean ridge basalt.

Figure 2: Characteristics of enriched mantle in kimberlites and oceanic volcanoes. a, ϵNd_i versus $(^{87}Sr/^{86}Sr)_i$ from kimberlites of the Kaapvaal craton[33] and Rajmahal, India[58], and basaltic volcanics from the Walvis Ridge[7,37] and the Indian Ocean—that is, the Kerguelen Plateau and the Christmas Island Seamount Province[8]; also shown are fields for kimberlites and EM1, PREMA and DM compositions[59]. **b,** Evolution of $(^{87}Sr/^{86}Sr)_i$ in perovskites from African kimberlites from ref.[34]; also shown is the MARID (mica-amphibole-rutile-ilmenite-diopside) end-member defined from kimberlite xenoliths (reflecting lithospheric mantle) and kimberlite melt end-member defined largely by PIC (phlogopite-ilmenite-clinopyroxene) xenoliths[22]. **c,** Evolution of ϵNd_i in Kaapvaal kimberlites[33]; solid red lines show statistically defined change points (using conjugate partitioned recursion) and two-sigma uncertainty bounds of the two averages (thin red lines) before and after the change point at 114 Ma[9]; this coincides with timing of lithospheric delamination (dashed vertical line at 114 Ma)[9]. **d,** Evolution of $(^{87}Sr/^{86}Sr)_i$ at Walvis Ridge[7,37]; **e,** Evolution of ϵNd_i at Walvis Ridge[7,37]; in both **d** and **e**, a change point occurs at 107 Ma, 13 Myr after accelerated rifting and exhumation at ~120 Ma (Extended Data Fig. 2); **f,** Frequency of individual dated volcanic samples from Walvis, with the earliest known volcanism occurring at 114 Ma (radiometric ages from refs.[7,37]).

Figure 3: Geodynamic simulations of convective erosion of lithospheric keels and lateral transport of removed domains. a, Simulations showing convective removal of lithospheric keels, which migrates toward cratonic interiors over time[9,10]; enriched material is removed and transported rift-ward and into the sub-oceanic asthenosphere (left of dashed line) where it is then transported upward by convection cells. **b,** Flow rate of decoupled lithospheric material—crossing a transect 200 km from the COB (see **a**)—into the sub-oceanic asthenosphere (SOA) over time, exhibiting pulsing behaviour. Three alternative models are shown (Methods) and a slow divergence scenario is also considered (Extended Data Fig. 3); the lower plot shows the cumulative frequency of SCLM entering the SOA for these different models, with the growth rate of this SCLM addition declining over time. **c,** Histogram and probability density function (PDF) of time estimates for decoupled SCLM to travel from the transect below the proto-rift (see **a**) to the base of the oceanic lithosphere (Extended Data Fig. 6) from two locations (150, 200 km from COB; see dashed line in **a**); panel **d** shows the same data as an empirical cumulative distribution function.

Figure 4: Eastern Indian Ocean Seamount Province as a test site for model evaluation. a, Plate tectonic reconstruction at 50 Ma (South Pole Lambert azimuthal equal-area projection) showing the age distribution of volcanic seamounts from refs.[8,41]. The grey arrow indicates the general age progression away from western Australia. The reconstruction was generated using GPlates software (https://www.gplates.org/), plotted in QGIS (https://qgis.org/). **b,** Present-day locations of the same seamounts in the eastern Indian Ocean, as shown in Fig. 5. The map background shows Global Multi-Resolution Topography (GMRT) from GeoMapApp (https://www.geomapapp.org/).

Figure 5: Temporal changes in enrichment within the Eastern Indian Ocean Seamount Province. a, $(^{208}Pb/^{204}Pb)_i$ versus $(^{206}Pb/^{204}Pb)_i$ of volcanics spanning the CHRISP[8] and the IFZ[41], coloured by age (n=31). The fields for EM1, lamproites, and kimberlites are from ref.[41], and another proposed EM1 composition (star) is from ref.[42]. **b,** $(^{206}Pb/^{204}Pb)_i$ of the above volcanics over time, coloured by ϵNd_i (n=30; data from refs.[8,41]), with the EM1 field[41] shown in pink. Linear regressions (n=1,000 from weighted bootstrap resampling procedure; see Methods) are shown in blue; samples give r^2 min/max: 0.34–0.91, median: 0.71. The data support the hypothesis that convective SCLM removal enriches the sub-oceanic asthenosphere, driving the early peak and gradual decline of enriched mantle components.

References

1. A. Zindler and S. Hart. Chemical geodynamics. *Annual Review of Earth and Planetary Sciences*, 14(1):493–571, 1986.
2. M. G. Jackson and R. Dasgupta. Compositions of HIMU, EM1, and EM2 from global trends between radiogenic isotopes and major elements in ocean island basalts. *Earth and Planetary Science Letters*, 276(1):175–186, 2008.
3. V. J. M. Salters and A. Sachi-Kocher. An ancient metasomatic source for the Walvis Ridge basalts. *Chemical Geology*, 273(3):151–167, 2010.

4. S. J. Turner, C. H. Langmuir, M. A. Dungan, and S. Escrig. The importance of mantle wedge heterogeneity to subduction zone magmatism and the origin of EM1. *Earth and Planetary Science Letters*, 472:216–228, 2017.
5. A. Stracke, A. W. Hofmann, and S. R. Hart. FOZO, HIMU, and the rest of the mantle zoo. *Geochemistry, Geophysics, Geosystems*, 6(5):Q05007, 2005.
6. X.-J. Wang, L.-H. Chen, A. W. Hofmann, F.-G. Mao, J.-Q. Liu, Y. Zhong, L.-W. Xie, and Y.-H. Yang. Mantle transition zone-derived EM1 component beneath NE China: Geochemical evidence from Cenozoic potassic basalts. *Earth and Planetary Science Letters*, 465:16–28, 2017.
7. K. Hoernle, J. Rohde, F. Hauff, D. Garbe-Schönberg, S. Homrighausen, R. Werner, and J. P. Morgan. How and when plume zonation appeared during the 132 Myr evolution of the Tristan Hotspot. *Nature Communications*, 6(1):7799, 2015.
8. K. Hoernle, F. Hauff, R. Werner, P. van den Bogaard, A. D. Gibbons, S. Conrad, and R. D. Müller. Origin of Indian Ocean Seamount Province by shallow recycling of continental lithosphere. *Nature Geoscience*, 4(12):883–887, 2011.
9. T. M. Gernon, S. M. Jones, S. Brune, T. K. Hincks, M. R. Palmer, J. C. Schumacher, R. M. Primiceri, M. Field, W. L. Griffin, S. Y. O'Reilly, D. Keir, C. J. Spencer, A. S. Merdith, and A. Glerum. Rift-induced disruption of cratonic keels drives kimberlite volcanism. *Nature*, 620(7973):344–350, 2023.
10. T. M. Gernon, T. K. Hincks, S. Brune, J. Braun, S. M. Jones, D. Keir, A. Cunningham, and A. Glerum. Coevolution of craton margins and interiors during continental break-up. *Nature*, 632(8024):327–335, 2024.
11. M. G. Jackson and F. A. Macdonald. Hemispheric geochemical dichotomy of the mantle is a legacy of austral supercontinent assembly and onset of deep continental crust subduction. *AGU Advances*, 3:e2022AV000664, 2022.
12. S. Homrighausen, K. Hoernle, H. Zhou, J. Geldmacher, J-A. Wartho, F. Hauff, R. Werner, S. Jung, and J. P. Morgan. Paired EMI-HIMU hotspots in the South Atlantic—Starting plume heads trigger compositionally distinct secondary plumes? *Science Advances*, 6(28):eaba0282, 2022.
13. N. Ussami, Carlos A. M. Chaves, L. S. Marques, and M. Ernesto. Origin of the Rio Grande Rise–Walvis Ridge reviewed integrating palaeogeographic reconstruction, isotope geochemistry and flexural modelling. *Geological Society, London, Special Publications*, 369(1):129–146, 2013.
14. W. M. White. Probing the Earth's deep interior through geochemistry. *Geochemical Perspectives*, 4(2):95–96, 2015.
15. S. Pilet, J. Hernandez, P. Sylvester, and M. Poujol. The metasomatic alternative for ocean island basalt chemical heterogeneity. *Earth and Planetary Science Letters*, 236(1):148–166, 2005.
16. S. F. Foley and T. P. Fischer. An essential role for continental rifts and lithosphere in the deep carbon cycle. *Nature Geoscience*, 10(12):897–902, 2017.
17. A. R. Guimarães, J. G. Fitton, L. A. Kirstein, and D. N. Barfod. Contemporaneous intraplate magmatism on conjugate South Atlantic margins: A hotspot conundrum. *Earth and Planetary Science Letters*, 536:116147, 2020.
18. T. M. Gernon, R. Barr, J. G. Fitton, T. K. Hincks, D. Keir, J. Longman, A. S. Merdith, R. N. Mitchell, and M. R. Palmer. Transient mobilization of subcrustal carbon coincident with Palaeocene–Eocene Thermal Maximum. *Nature Geoscience*, 15:573–579, 2022.
19. L. T. Elkins-Tanton. Continental magmatism, volatile recycling, and a heterogeneous mantle caused by lithospheric gravitational instabilities. *Journal of Geophysical Research: Solid Earth*, 112(B3):B03405, 2007.
20. C. J. Hawkesworth, M. S. M. Mantovani, P. N. Taylor, and Z. Palacz. Evidence from the Parana of south Brazil for a continental contribution to Dupal basalts. *Nature*, 322(6077):356–359, 1986.
21. D. McKenzie and R. K. O'Nions. The source regions of ocean island basalts. *Journal of Petrology*, 36(1):133–159, 1995.
22. A. Fitzpayne, A. Giuliani, R. Maas, J. Hergt, P. Janney, and D. Phillips. Progressive metasomatism of the mantle by kimberlite melts: Sr–Nd–Hf–Pb isotope compositions of MARID and PIC minerals. *Earth and Planetary Science Letters*, 509:15–26, 2019.
23. R. Huismans and C. Beaumont. Depth-dependent extension, two-stage breakup and cratonic underplating at rifted margins. *Nature*, 473(7345):74–78, 2011.
24. B. B. Hanan and J.-G. Schilling. The dynamic evolution of the Iceland mantle plume: the lead isotope perspective. *Earth and Planetary Science Letters*, 151(1):43–60, 1997.
25. C.-Z. Liu, H. J. B. Dick, R. N. Mitchell, W. Wei, Z.-Y. Zhang, A. W. Hofmann, J.-F. Yang, and Y. Li. Archean cratonic mantle recycled at a mid-ocean ridge. *Science Advances*, 8(22):eabn6749, 2022.
26. S. D. King and D. L. Anderson. Edge-driven convection. *Earth and Planetary Science Letters*, 160(3):289–296, 1998.
27. S. D. King and J. Ritsema. African hot spot volcanism: Small-scale convection in the upper mantle beneath cratons. *Science*, 290(5494):1137–1140, 2000.
28. A. Manjón-Cabeza Córdoba and M. D. Ballmer. The role of edge-driven convection in the generation of volcanism – Part 1: A 2D systematic study. *Solid Earth*, 12(3):613–632, 2021.
29. D. L. Anderson. The persistent mantle plume myth. *Australian Journal of Earth Sciences*, 60(6-7):657–673, 2013.
30. X. Bao, C. R. Lithgow-Bertelloni, M. G. Jackson, and B. Romanowicz. On the relative temperatures of Earth's volcanic hotspots and mid-ocean ridges. *Science*, 375(6576):57–61, 2022.
31. M. J. Raddick, E. M. Parmentier, and D. S. Scheirer. Buoyant decompression melting: A possible mechanism for intraplate volcanism. *Journal of Geophysical Research: Solid Earth*, 107(B10):2228, 2002.
32. S. Tappe, K. Smart, T. Torsvik, M. Massuyeau, and M. de Wit. Geodynamics of kimberlites on a cooling Earth: Clues to plate tectonic evolution and deep volatile cycles. *Earth and Planetary Science Letters*, 484:1–14, 2018.
33. G. M. Nowell, D. G. Pearson, D. R. Bell, R. W. Carlson, C. B. Smith, P. D. Kempton, and S. R. Noble. Hf isotope systematics of kimberlites and their megacrysts: New constraints on their source regions. *Journal of Petrology*, 45(8):1583–1612, 2004.
34. J. Woodhead, J. Hergt, D. Phillips, and C. Paton. African kimberlites revisited: In situ Sr-isotope analysis of groundmass perovskite. *Lithos*, 112:311–317, 2009.
35. C. B. Smith. Pb, Sr and Nd isotopic evidence for sources of southern African Cretaceous kimberlites. *Nature*, 304(5921):51–54, 1983.
36. J. Hu, L. Liu, M. Faccenda, Q. Zhou, K. M. Fischer, S. Marshak, and C. Lundstrom. Modification of the Western Gondwana craton by plume–lithosphere interaction. *Nature Geoscience*, 11(3):203–210, 2018.
37. S. Homrighausen, K. Hoernle, F. Hauff, J. A. Wartho, P. van den Bogaard, and D. Garbe-Schönberg. New age and geochemical data from the Walvis Ridge: The temporal and spatial diversity of South Atlantic intraplate volcanism and its possible origin. *Geochimica et Cosmochimica Acta*, 245:16–34, 2019.
38. S. Brune, S. E. Williams, N. P. Butterworth, and R. D. Müller. Abrupt plate accelerations shape rifted continental margins. *Nature*, 536(7615):201–204, 2016.
39. J. Rohde, K. Hoernle, F. Hauff, R. Werner, J. O'Connor, C. Class, D. Garbe-Schönberg, and W. Jokat. 70 ma chemical zonation of the Tristan-Gough hotspot track. *Geology*, 41(3):335–338, 3/17/2025 2013.
40. J. T. VanderPlas. Understanding the Lomb–Scargle periodogram. *The Astrophysical Journal Supplement Series*, 236(16):1–26, 2018.
41. A. Dürkefälden, F. Hauff, K. Hoernle, M. Portnyagin, J.-A. Wartho, D. Garbe-Schönberg, A. Gurenko, P. van den Bogaard, A. Kipf, and M. Gutjahr. Geochemical and temporal evolution of Indian MORB mantle revealed by the Investigator Ridge in the NE Indian Ocean. *Gondwana Research*, 134:347–364, 2024.
42. S. Homrighausen, K. Hoernle, F. Hauff, P. A. Hoyer, K. M. Haase, W. H. Geissler, and J. Geldmacher. Evidence for compositionally distinct upper mantle plumelets since the early history of the Tristan-Gough hotspot. *Nature Communications*, 14(1):3908, 2023.
43. B. Dupré and C. J. Allègre. Pb–Sr isotope variation in Indian Ocean basalts and mixing phenomena. *Nature*, 303(5913):142–146, 1983.
44. J. J. Mahoney, W. M. White, B. G. J. Upton, C. R. Neal, and R. A. Scrutton. Beyond EM-1: Lavas from Afanasy-Nikitin Rise and the Crozet Archipelago, Indian Ocean. *Geology*, 24(7):615–618, 1996.
45. A. Y. Borisova, B. V. Belyatsky, M. V. Portnyagin, and N. M. Sushchevskaya. Petrogenesis of olivine-phyric basalts from the Aphanasey Nikitin Rise: Evidence for contamination by cratonic lower continental crust. *Journal of Petrology*, 42(2):277–319, 2001.
46. B. B. Hanan, J. Blichert-Toft, D. G. Pyle, and D. M. Christie. Contrasting origins of the upper mantle revealed by hafnium and lead isotopes from

the Southeast Indian Ridge. *Nature*, 432(7013):91–94, 2004.
47. S. Escrig, F. Capmas, B. Dupré, and C. J. Allègre. Osmium isotopic constraints on the nature of the DUPAL anomaly from indian mid-ocean-ridge basalts. *Nature*, 431(7004):59–63, 2004.
48. S. Homrighausen, K. Hoernle, J. A. Wartho, F. Hauff, and R. Werner. Do the 85 °E Ridge and Conrad Rise form a hotspot track crossing the Indian Ocean? *Lithos*, 398-399:106234, 2021.
49. R. D. Müller, S. Zahirovic, S. E. Williams, J. Cannon, M. Seton, D. J. Bower, M. G. Tetley, C. Heine, E. Le Breton, S. Liu, S. H. J. Russell, T. Yang, J. Leonard, and M. Gurnis. A global plate model including lithospheric deformation along major rifts and orogens since the Triassic. *Tectonics*, 38(6):1884–1907, 2019.
50. E. R. Humphreys and Y. Niu. On the composition of ocean island basalts (OIB): The effects of lithospheric thickness variation and mantle metasomatism. *Lithos*, 112(1):118–136, 2009.
51. F. A. Capitanio, O. Nebel, and P. A. Cawood. Thermochemical lithosphere differentiation and the origin of cratonic mantle. *Nature*, 588(7836):89–94, 2020.
52. D. G. Pearson, J. M. Scott, J. Liu, A. Schaeffer, L. H. Wang, J. van Hunen, K. Szilas, T. Chacko, and P. B. Kelemen. Deep continental roots and cratons. *Nature*, 596(7871):199–210, 2021.
53. S. R. Hart. A large-scale isotope anomaly in the Southern Hemisphere mantle. *Nature*, 309(5971):753–757, 1984.
54. M. De Witt, M. Jeffery, H. Bergh, and L. Nicolaysen. *Geological map of sectors of Gondwana reconstructed to their disposition*. American Association of Petroleum Geologists, South Boulder, Tulsa, OK, 1988.
55. M. Mazzucchelli, A. Cipriani, C. Hémond, A. Zanetti, G. W. Bertotto, and C. A. Cingolani. Origin of the DUPAL anomaly in mantle xenoliths of Patagonia (Argentina) and geodynamic consequences. *Lithos*, 248-251:257–271, 2016.
56. S. L. Goldstein, G. Soffer, C. H. Langmuir, K. A. Lehnert, D. W. Graham, and P. J. Michael. Origin of a 'Southern Hemisphere' geochemical signature in the Arctic upper mantle. *Nature*, 453(7191):89–93, 2008.
57. J. G. Fitton. *The OIB paradox*, volume 430, pages 387–412. Geological Society of America, 2007.
58. A. Kumar, A. M. Dayal, and V. M. Padmakumari. Kimberlite from Rajmahal magmatic province: Sr-Nd-Pb isotopic evidence for Kerguelen plume derived magmas. *Geophysical Research Letters*, 30(20):2053, 2003.
59. H. Rollinson and V. Pease. *Using Geochemical Data*. Cambridge University Press, Cambridge, 2 edition, 2021.

Methods

Geodynamic models

Our thermo-mechanical simulations used the geodynamic tool ASPECT (Advanced Solver for Planetary Evolution, Convection, and Tectonics), a finite element code to simulate convection in Earth's mantle and lithospheric deformation[60,61,62,63,64,65]. This tool was used to compute the dynamic evolution of the continental lithosphere and the asthenosphere over a ~100 Myr period (Figs. 3a–b). The software operates by solving the conservation equations of energy, mass and momentum for Earth materials experiencing viscoplastic deformation[66]. We apply rheologies that account for temperature, pressure, and strain-rate dependent flow laws and include strain weakening mechanisms[9].

The models are kinematically driven by imposing velocity boundary conditions at the left and right sides. The simulation creates a rift that migrates laterally[67], delaying lithospheric breakup. The asthenosphere exhibits strong rotational flow patterns due to pressure gradients beneath the rift. The steep lithospheric gradients generated by rifting lead to the edge-driven convection and Rayleigh-Taylor instabilities that migrate cratonward. We next elaborate on the model geometry, the thermo-mechanical setup as well as the limitations of the model.

The model domain comprises 120 and 800 elements in the vertical and horizontal directions, respectively, and is 300 km deep as well as 2,000 km wide. Four uniform layers make up the initial distribution of material: an upper crust that is 20 km thick, a lower crust that is 15 km thick, a mantle lithosphere that is 125 km thick, and an asthenosphere that is 140 km thick. We initiate rifting in a predetermined area, by defining a domain in model centre where the crust is 5 km thicker and the mantle lithosphere is 25 km thinner than in the surrounding lithosphere, which represents mobile belt conditions typical for locations where intracontinental rifts form[68]. Due to initial thermal equilibration, these conditions induce a thermo-mechanical weakness. Over a distance of 200 km, these layer thicknesses gradually transition to the ambient lithosphere. We track the evolution of the material within a 30 km thick asthenospheric layer beneath some portions of the lithosphere as a simplified representation of the weak metasomatised lithospheric keel. A thickness of 30 km for this layer was chosen to represent the vertical extent of the thermal boundary layer (TBL), which xenolith and geotherm analyses suggest is approximately 30–35 km thick, irrespective of the total thickness of the lithosphere[9]. Our models assume a 160 km depth of the thermal lithosphere-asthenosphere boundary across the continent, with ~20 km thinning in the mobile belt later exploited by the rift. While this configuration does not capture all regional variations, it is consistent with inferred lithosphere-asthenosphere boundary depths beneath most kimberlites emplaced over the past 250 million years[9], suggesting it is not an unreasonable approximation for our study.

The flow laws of each layer represent, respectively, the upper crust, lower crust, mantle lithosphere, and asthenosphere, as wet quartzite[69], wet anorthite[70], dry olivine[71] , and wet olivine[71] (see ref.[9] for thermo-mechanical parameters). Prior sensitivity analysis shows that varying viscosity of the lithospheric thermal boundary layer and the asthenosphere within a realistic range does not have a significant impact on the wavelength (42–65 km) or propagation rate (14–33 km/Myr) of Rayleigh-Taylor instabilities—the key variables of interest. Rayleigh-Taylor instabilities are primarily driven by density contrasts; viscosity variations, while influential, are not the dominant control. Nonetheless, we conducted 28 additional sensitivity experiments to ascertain how co-variation in density and viscosity affects decoupling, entrainment, and transport processes, along with their characteristic timescales (see below). Our model includes a piece-wise linear function to account for strain-dependent friction softening: (a) the friction coefficient linearly decreases by up to 75% between a brittle strain range of 0 and 1; (b) the friction coefficient remains constant for strains >1. Analogously, we account for viscous strain-dependent weakening via a linear reduction of the viscosity up to 75% within a range of the viscous strain between 0 and 1.

In the asthenosphere, we adopt an activation energy of 480 kJ mol^{-1}. The impact of changing the asthenospheric activation energy on the migration of instabilities and the process of convective removal was explored in prior work[9] and is now sum-

marised. Sublithospheric viscosity, particularly its dependence on activation energy, plays a crucial role in the development of mantle instabilities. Shallow-asthenosphere viscosity is primarily governed by dislocation creep, consistent with observations of seismic anisotropy in the upper mantle. We adopt experimentally derived flow laws of wet olivine dislocation creep with an activation energy of 480 ± 40 kJ mol^{-1} (ref. [71]). These values are well within the independently determined range of 360–540 kJ mol^{-1} (ref. [72]). To assess model robustness, we performed additional simulations varying activation energy within experimental uncertainties while keeping all other parameters constant. Lowering the activation energy to 440 kJ mol^{-1} reduces viscosity in the shallow asthenosphere and thermal boundary layer by approximately a factor of two. This increases the lateral propagation and migration rates of instabilities by a similar factor. Increasing the activation energy to 530 kJ mol^{-1} leads to a viscosity increase that prevents the formation of Rayleigh-Taylor instabilities. We conclude that dripping of metasomatised material is possible only for sufficient low viscosities of the cratonic keels (the regime threshold is examined further, as described below). If dripping takes place, however, it migrates along the base of the craton at a rate that is inversely proportional to the keel viscosity [9].

We employ velocity boundary conditions with a 10 mm/yr extension rate. We fix the right-hand side of the model for simplicity through a free-slip boundary condition and no material inflow. However, we confirmed that even if extension velocities are distributed symmetrically at both side boundaries, our findings remain the same. A continual input of material via the lower boundary counterbalances the material outflux through the left boundary. This influx rate through the lower boundary (1.5 mm/yr) is derived from the ratio between horizontal and vertical model extent multiplied by the imposed divergence rate. In contrast to the lower boundary, a free surface is used at the upper boundary meaning that this boundary is free of tractions, able to distort and without any in or outflow of mass [65].

The lateral borders are thermally insulated, and the bottom and surface temperatures are respectively maintained at 1,420°C and 0°C. The distribution of temperature is initially balanced along 1D columns by equilibrating the temperature field accounting for the contribution of thermal boundary conditions, radiogenic heat production, heat capacity, and thermal diffusivity. Here, we set the initial depth of the compositional lithosphere-asthenosphere-boundary at a temperature of 1,350°C to equal the bottom of the conductive lithosphere. In the sub-lithosphere domain, the initial temperature increases adiabatically with depth. We further equilibrate the entire temperature distribution of the model for 30 Myr prior to the start of extension in order to smooth the change in the thermal gradient between the lithosphere and asthenosphere.

The following model assumptions need to be taken into consideration when evaluating our findings: (1) Chemical changes, melt production, and magma ascent are not explicitly taken into account as we concentrate on first-order thermo-mechanical processes. Specifically, we examine the distribution of 'tracer' material—the removed portions of the metasomatised lithospheric keel—through time and space. This material is available for melting in the asthenosphere where decompression is expected to occur beneath young, thin oceanic lithosphere. While we estimate the timescales for this SCLM material to reach the surface via convective upwelling (Extended Data Fig. 6), our ASPECT models cannot currently be implemented to resolve their chemical or melting properties. However, we do not think that the omission of melting materially weakens our main conclusions. Its primary effect—reducing viscosity in the lower lithosphere—would likely enhance, rather than hinder, the invoked delamination process. Indeed, previous studies show that viscosity reductions due to partial melting can weaken the lithosphere [73]. This effect, combined with density contrasts arising from temperature differences across the TBL [9], would only act to augment keel removal. With regards to the melting processes within the asthenosphere, further work is needed to incorporate melting into geodynamic models in a way that balances realism with uncertainty, reflecting our incomplete understanding of such compositionally and rheologically complex natural systems.

(2) Our general modelling approach omits processes associated with mantle plumes, along-strike lithospheric heterogeneities, and large-scale mantle flow patterns. This is appropriate for our setup because we focus on the removal and lateral transport of continental keel material within the upper mantle, rather than deep mantle dynamics. A deeper domain with an open lower boundary would likely introduce additional complexities beyond the scope of our study, such as whole-mantle circulation effects, which are not required to capture the primary processes of interest. Nonetheless, we conducted further tests to explore the possible impact of a deeper model domain on the scale and spacing of Rayleigh-Taylor instabilities [10], finding that these did not change significantly (see below). Further, in nature, the lateral mantle flow, or mantle wind, will vary by location, but in many cases, its motion — e.g., the westward flow beneath Africa — will help transport decoupled SCLM domains into the sub-oceanic asthenosphere. Nonetheless, further research is needed to assess how their formation and migration interact with deeper mantle upwellings, a question beyond the scope of this study.

(3) We assume, for simplicity, that the lithosphere-asthenosphere boundary's initial depth does not vary on a scale of a thousand kilometres. We confirmed that the presence of a sloping lithosphere-asthenosphere boundary and changes in the lithospheric thickness between models did not affect our conclusions. We also conducted experiments extending the vertical extent of the model domain to 410 km, assessing whether this change significantly impacts the scale, spacing, or speed of Rayleigh-Taylor instabilities—the primary mechanism of convective removal and transport in our models. Here, we found that the distance between two Rayleigh-Taylor instabilities does not increase proportionally to the height of the convection cell. Despite the 410-model having convection cells approximately twice as high as the reference model, the distance between instabilities—when measured at the depth of the TBL (that is, the metasomatised layer which is beige in the animation)—remains remarkably similar. The drips maintain a similar width at the level of the TBL, irrespective of whether

the convection cells are large or small (i.e., the mean spacings for the reference model and 410-model are 269 km and 255 km, respectively). For the models to be meaningful, the TBL just needs to be thin compared to the height of the convection cell—a criterion met in all cases described in our paper.

To assess the impact of the prescribed plate kinematics of the model, we introduced symmetric boundary conditions (Supplementary Video 1), and both varied the extension velocity (5 mm/yr and 20 mm/yr instead of 10 mm/yr in the reference model; Supplementary Videos 2 and 3), and explored the influence of time-dependent extension velocities. In the latter case, we conducted two model runs where the extension rate increases through time. We consider (1) Slow divergence of 3 mm/yr for the first 5 Myr of rifting followed by fast divergence of 14 mm/yr until the end of the model run (Supplementary Video 4); and (2) Slow divergence of 5 mm/yr for 20 Myr of rifting followed by fast divergence of 20 mm/yr until the end of the model run (Supplementary Video 5). Again, the key process of sequential delamination occurs in all scenarios as described in the reference model. Migration rates differ slightly from the reference model but are in full agreement with observational constraints.

Finally, we conducted 28 simulations to assess how the covariation in density and viscosity of the metasomatised lithospheric keel influence its evolution during continental rifting and breakup. In each model, only the keel's reference density (ρ_0) and activation energy—a key parameter in computing viscosity—were varied, while all other parameters remained consistent with the reference case (Fig. 3), which is indicated with the dashed rectangle in Extended Data Fig. 5. The SCLM keel density was systematically varied from 3,250 to 3,350 kg m^{-3}, spanning a range of ±1.5% relative to the asthenosphere. Each model is shown 50 Myr after rift onset, with keel density (colour) overlain by viscosity (greyscale) to visualise both fields within a single frame (Extended Data Fig. 5). The experiments identify three distinct behavioural regimes (see main text) and demonstrate that most scenarios result in lithospheric material entering the sub-oceanic asthenosphere, though on different timescales—an outcome that can be tested in future studies.

Quantifying the tempo of material transfer

Using simulation outputs, we quantify the amount of decoupled lithospheric material that enters into the sub-oceanic asthenosphere over time. To do this, we compute the vertical integral of the flow rate of decoupled metasomatised lithosphere (extracted from ASPECT using the open-source data analysis and visualisation application, ParaView[74]). We first multiply the fraction of this material with the horizontal velocity component. We integrate this value vertically and rescale it so that the numbers correspond to the total thickness of material (that is, beige decoupled SCLM; see Fig. 3) that passes through a line at a given x-location per output time step. The x-locations where measurements are made are located close to the lithospheric discontinuity at 150 km and 200 km from the COB as shown in Fig. 3a. The rescaled flow rate values are meters per 0.5 million years (the visualisation output time step), which for simplicity is doubled and plotted as m Myr^{-1} (Fig. 3b). We also calculate the cumulative amount of this material over time (Fig. 3b). Using the flow rate values for both the 150 km and 200 km profiles, we applied a Lomb–Scargle periodogram—an algorithm commonly used to detect and characterise periodic signals in unevenly sampled data[40,75,76]. We perform this analysis in the open-source statistical programming language, R, using the data visualisation package, ggplot2, and library 'lomb'. This approach is used to diagnose statistically significant signals at 5 to 6 Myr periods (Extended Data Fig. 4). We computed P-values for the peak amplitude in the periodogram from the exponential distribution[77].

An important consideration is whether the pulsing of decoupled SCLM (Fig. 3b) is a model artefact, though we consider this unlikely. In our models, the lithospheric keel (shown in beigeoin Fig. 3a) is continuous along the lithospheric root, except where it is thinned beneath the rift. It is not distributed in a manner that would introduce artificial cyclicity. Instead, our analysis of Rayleigh-Taylor instabilities indicates that pulsed outputs in our model (Fig. 3b; Extended Data Fig. 4) are related to edge-driven convection[26,27]. Specifically, steep lithosphere-asthenosphere boundary gradients introduce pronounced horizontal temperature contrasts, where upwelling asthenosphere cools adjacent to the lithosphere, increasing viscosity and density. This density contrast induces gravitational 'dripping', which—due to the higher viscosity—occurs in discrete events (Extended Data Fig. 4).

Finally, it is important to establish how long it would take enriched material (that is, decoupled lithospheric material) to be detectable in surface volcanism, once it has first crossed into the asthenospheric mantle. This would approximate the time lag expected between full continental breakup (when enriched decoupled lithosphere enters the sub-oceanic asthenosphere) and EM1-type volcanism. To estimate this, we used simple Monte Carlo simulations to sample the length-scales of typical convection cells forming near to the lithospheric discontinuity and maximum mantle flow velocities in our ASPECT simulations (Extended Data Fig. 6) to compute a range of lag times considered most likely (Fig. 3c–d). We plot the results as a histogram and probability density function (PDF; Fig. 3c), and as an empirical cumulative distribution function (Fig. 3d). This analysis suggests lag times ranging from 5 to 14.5 Myr, with a median of 8.0 and a mean of 8.7 Myr.

Geochemical data analysis

To test our geodynamic model, we first compiled isotopic data from the eastern Indian Ocean Seamount Province, encompassing the Christmas Island Seamount Province (CHRISP)[8] and the Investigator Fracture Zone (IFZ)[41] (Fig. 4). The wider CHRISP region, where volcanoes formed nearer to the continental margins following India-Australia breakup at ~126 Ma (Fig. 4a), exhibits strong EM1-type signatures[8,41] and lacks any known deep plumes[30], allowing mantle enrichments to be unequivocally linked to processes along nearby continents[8]. The post-breakup volcanism in the CHRISP, spanning 116 Ma to 37 Ma, is well documented by Hoernle et al. (2011)[8], with 26 radiometric ages and an array of Sr-Nd-Pb-Hf isotopes (Figs.

4–5). We exclude the youngest phase (4–4.5 Ma) from Christmas Island's Upper Volcanic Series[8] due to its proximity (i.e., relative to earlier magmatic phases; Fig. 4a) to the Sunda-Java subduction zone (Fig. 4b), where related crustal and tectonic processes have been implicated in that renewed melting phase[78]. The IFZ volcanoes, described by Dürkenfälden et al. (2024)[41], include five radiometric ages and a comparable isotopic dataset. We reconstructed the locations of these sites at 50 Ma (Fig. 4a) using the open-source plate-tectonic software, GPlates (https://www.gplates.org/).

Many data points in our compilation originate from broadly the same borehole or region (Extended Data Fig. 1). To mitigate sampling bias, we applied weighted bootstrap resampling following the procedure outlined by Keller and Schoene[79], using the equation:

$$W_i \propto 1 \Big/ \sum_{j=1}^{n} \left(\frac{1}{\left(\frac{z_i - z_j}{a}\right)^2 + 1} + \frac{1}{\left(\frac{t_i - t_j}{b}\right)^2 + 1} \right)$$

where n is the number of original observations (i.e., samples in the compilation), z is the spatial location, t is the radiometric age of the rock and (a,b) are the normalisation coefficients. For the latter, we apply a distance coefficient a=100 km to account for closely spaced drilling sites, and a time coefficient b=5 Myr, which exceeds the typical age uncertainty of the samples.

We performed 1,000 iterations, each involving weighted sampling of n points with replacement. We then calculate regression parameters for each sample set. The resulting linear regressions and corresponding R^2 values are shown in Fig. 5b–c. This provides an estimate of uncertainty in the relationship between isotope ratio and age.

For a comparison exercise, we also compiled isotopic data from oceanic basalts geographically spanning the Broken Ridge, Ninety East Ridge, and Kerguelen Plateau in the Indian Ocean (Extended Data Figs. 1). These volcanoes have been heavily sampled by ocean drilling expeditions, providing a reasonably continuous, well-dated sequence of ocean island magmatism from 120–0 Ma (Extended Data Fig. 8). We also studied contemporaneous kimberlites from southern Africa and India (Fig. 2a). The original positions of these sites are shown in Extended Data Fig. 8a, reconstructed using GPlates.

For the time series analysis, we used samples with well-accepted radiometric ages acquired from several IODP expeditions (Supplementary Data Tables 1–3). The data are summarised in Extended Data Fig. 8b (Kerguelen), which shows the variation in $(^{206}Pb/^{204}Pb)_i$ over time, coloured by ϵNd_i, where

$$\varepsilon_{Nd} = \left(\frac{\left(\frac{^{143}Nd}{^{144}Nd}\right)_{\text{sample}}}{\left(\frac{^{143}Nd}{^{144}Nd}\right)_{\text{CHUR}}} - 1 \right) \times 10^4$$

where CHUR refers to the isotopic ratio of the CHondritic Uniform Reservoir.

In a separate analysis investigating the onset of volcanism at Walvis Ridge and its relation to contemporaneous kimberlite volcanism in Africa, we performed conjugate partitioned recursion (CPR)[80] to detect whether any step changes are present in the isotope datasets for Walvis Ridge[7,37] (Fig. 2d). This approach, deployed in the numeric computing platform, MATLAB, applies an iterative algorithm involving binary partitioning by marginal likelihood and conjugate priors to identify an unknown number of change-points[80]. In the case that a marginal likelihood favors a change-point model, the CPR algorithm defines a change point and two-sigma uncertainty bounds of the two averages before and after the change point[80]. Previously, we used this approach to show a change point in $(^{87}Sr/^{86}Sr)_i$ and ϵNd_i in southern African kimberlites occurs at 117 and 114 Ma (Figs. 2b–d), which coincides with inferred delamination of the lithospheric keel of the Kaapvaal craton[9]. Using the same procedure, we identified a step change in ϵNd_i at the Walvis Ridge occurs between 112 and 107 Ma (Fig. 2d); >2 Myr after the recorded onset of volcanism there (Fig. 2e).

Additional references are cited in the Extended Data Figures[81,82,83,84,85,86,87,88,89,90] and Supplementary Data Files[91,92,93,94,95,96,97,98,99,100,101,102].

Data Availability

All data related to this manuscript can be found in the Supplementary Tables and are also available via Figshare at https://doi.org/10.6084/m9.figshare.30086716 (ref. [103]). Source data are provided with this paper.

Code Availability

The input file, custom source code, and ASPECT installation details for the thermo-mechanical simulations used in this study are available at the Zenodo repository: https://www.doi.org/10.5281/zenodo.7825780 (ref. [64]).

References

60. M. Kronbichler, T. Heister, and W. Bangerth. High accuracy mantle convection simulation through modern numerical methods. *Geophysical Journal International*, 191(1):12–29, 2012.
61. W. Bangerth and T. Heister. Aspect v1.4.0, 2016.
62. W. Bangerth, J. Dannberg, M. Fraters, R. Gassmoeller, A. Glerum, T. Heister, and J. Naliboff. ASPECT: Advanced Solver for Problems in Earth's ConvecTion, User Manual. https://doi.org/10.6084/m9.figshare.4865333.v8, 2021.
63. T. Heister, J. Dannberg, R. Gassmöller, and W. Bangerth. High accuracy mantle convection simulation through modern numerical methods–II: realistic models and problems. *Geophysical Journal International*, 210(2):833–851, 2017.
64. A. Glerum. Input file, custom source code and ASPECT installation details for the thermomechanical simulations in Gernon et al. (2023). https://doi.org/10.5281/zenodo.8185948, 2023.
65. I. Rose, B. Buffett, and T. Heister. Stability and accuracy of free surface time integration in viscous flows. *Physics of the Earth and Planetary Interiors*, 262:90–100, 2017.
66. A. Glerum, C. Thieulot, M. Fraters, C. Blom, and W. Spakman. Nonlinear viscoplasticity in ASPECT: benchmarking and applications to subduction. *Solid Earth*, 9(2):267–294, 2018.
67. S. Brune, C. Heine, M. Pérez-Gussinyé, and S. V. Sobolev. Rift migration explains continental margin asymmetry and crustal hyper-extension. *Nature Communications*, 5(1):4014, 2014.
68. M. E. Pasyanos, T. G. Masters, G. Laske, and Z. Ma. LITHO1.0: An updated crust and lithospheric model of the Earth. *Journal of Geophysical Research: Solid Earth*, 119(3):2153–2173, 2014.

69. E. H. Rutter and K. H. Brodie. Experimental grain size-sensitive flow of hot-pressed Brazilian quartz aggregates. *Journal of Structural Geology*, 26(11):2011–2023, 2004.
70. E. Rybacki, M. Gottschalk, R. Wirth, and G. Dresen. Influence of water fugacity and activation volume on the flow properties of fine-grained anorthite aggregates. *Journal of Geophysical Research: Solid Earth*, 111(B3), 2006.
71. G. Hirth and D. Kohlstedt. Rheology of the upper mantle and the mantle wedge: A view from the experimentalists. In J. Eiler, editor, *Inside the Subduction Factory*, pages 83–105. American Geophysical Union (AGU), 2004.
72. J. van Hunen, S. Zhong, N. M. Shapiro, and M. H. Ritzwoller. New evidence for dislocation creep from 3-D geodynamic modeling of the Pacific upper mantle structure. *Earth and Planetary Science Letters*, 238(1):146–155, 2005.
73. T. Gerya. Large-scale-long-term strength of the lithosphere: New theory and applications. *Petrology*, 32(1):128–141, 2024.
74. J. Ahrens, B. Geveci, and C. Law. *ParaView: An End-User Tool for Large Data Visualization*. Elsevier, 2005.
75. N. R. Lomb. Least-squares frequency analysis of unequally spaced data. *Astrophysics and Space Science*, 39(2):447–462, 1976.
76. J. D. Scargle. Studies in astronomical time series analysis. II. Statistical aspects of spectral analysis of unevenly spaced data. *The Astrophysical Journal*, 263(2):835–853, 1982.
77. W. H. Press, S. A. Teukolsky, S. T. Vetterling, and B. P. Flannery. *Numerical recipes in C: the art of scientific computing*. Cambridge University Press, Cambridge, 2 edition, 1994.
78. R. Taneja, C. O'Neill, M. Lackie, T. Rushmer, P. Schmidt, and F. Jourdan. 40Ar/39Ar geochronology and the paleoposition of Christmas Island (Australia), Northeast Indian Ocean. *Gondwana Research*, 28(1):391–406, 2015.
79. C. B. Keller and B. Schoene. Statistical geochemistry reveals disruption in secular lithospheric evolution about 2.5 Gyr ago. *Nature*, 485(7399):490–493, 2012.
80. G. Jensen. Closed-form estimation of multiple change-point models. *PeerJ Preprints*, 1:e90v3, 2013.
81. D. Hasterok, J. A. Halpin, A. S. Collins, M. Hand, C. Kreemer, M. G. Gard, and S. Glorie. New maps of global geological provinces and tectonic plates. *Earth-Science Reviews*, 231:104069, 2022.
82. B. V. da Silva, P. C. Hackspacher, M. C. S. Ribeiro, U. A. Glasmacher, A. O. Gonçalves, C. Doranti-Tiritan, D. F. de Godoy, and R. R. Constantino. Evolution of the Southwestern Angolan Margin: episodic burial and exhumation is more realistic than long-term denudation. *International Journal of Earth Sciences*, 108(1):89–113, 2019.
83. A. Margirier, J. Braun, C. Gautheron, J. Carcaillet, S. Schwartz, R. Pinna Jamme, and J. Stanley. Climate control on Early Cenozoic denudation of the Namibian margin as deduced from new thermochronological constraints. *Earth and Planetary Science Letters*, 527:115779, 2019.
84. G. Baby. *Mouvements verticaux des marges passives d'Afrique australe depuis 130 Ma, étude couplée: stratigraphie de bassin – analyse des formes du relief*. PhD thesis, Université de Rennes, 2017.
85. Y. H. Poudjom Djomani, S. Y. O'Reilly, W. L. Griffin, and P. Morgan. The density structure of subcontinental lithosphere through time. *Earth and Planetary Science Letters*, 184(3):605–621, 2001.
86. W. L. Griffin and S. Y. O'Reilly. Cratonic lithospheric mantle: Is anything subducted? *Episodes*, 30(1):43–53, 2007.
87. C.-T. A. Lee, P. Luffi, and E. J. Chin. Building and destroying continental mantle. *Annual Review of Earth and Planetary Sciences*, 39(39):59–90, 2011.
88. T. Furman, W. R. Nelson, and L. T. Elkins-Tanton. Evolution of the East African rift: Drip magmatism, lithospheric thinning and mafic volcanism. *Geochimica et Cosmochimica Acta*, 185:418–434, 2016.
89. B. Steinberger. Topography caused by mantle density variations: observation-based estimates and models derived from tomography and lithosphere thickness. *Geophysical Journal International*, 205(1):604–621, 2016.
90. Y. Wang, L. Liu, and Q. Zhou. Topography and gravity reveal denser cratonic lithospheric mantle than previously thought. *Geophysical Research Letters*, 49(1):e2021GL096844, 2022.
91. C. R. Neal, J. J. Mahoney, and W. J. Chazey. Mantle sources and the highly variable role of continental lithosphere in basalt petrogenesis of the Kerguelen Plateau and Broken Ridge LIP: Results from ODP Leg 183. *Journal of Petrology*, 43(7):1177–1205, 2002.
92. I. G. Nobre Silva, D. Weis, J. S. Scoates, and J. Barling. The Ninetyeast Ridge and its relation to the Kerguelen, Amsterdam and St. Paul hotspots in the Indian Ocean. *Journal of Petrology*, 54(6):1177–1210, 2013.
93. F. A. Frey and D. Weis. Temporal evolution of the Kerguelen plume: Geochemical evidence from 38 to 82 Ma lavas forming the Ninetyeast Ridge. *Contributions to Mineralogy and Petrology*, 121(1):12–28, 1995.
94. A.D. Saunders, M. Storey, I. L. Gibson, P. Leat, J. Hergt, and R.N. Thompson. Chemical and isotopic constraints on the origin of basalts from Ninetyeast Ridge, Indian Ocean: results from DSDP Legs 22 and 26 and ODP Leg 121. In J. Weissel, J. Peirce, E. Taylor, and J. Alt et al., editors, *ODP, Scientific results, Leg 121, Broken Ridge and Ninetyeast Ridge*, volume 121. Proceedings of the Ocean Drilling Program, 1991.
95. F. A. Frey, K. Nicolaysen, B. K. Kubit, D. Weis, and A. Giret. Flood basalt from Mont Tourmente in the Central Kerguelen Archipelago: the change from transitional to alkalic basalt at ~25 Ma. *Journal of Petrology*, 43(7):1367–1387, 2002.
96. S. Doucet, D. Weis, J. S Scoates, V. Debaille, and A. Giret. Geochemical and Hf–Pb–Sr–Nd isotopic constraints on the origin of the Amsterdam–St. Paul (Indian Ocean) hotspot basalts. *Earth and Planetary Science Letters*, 218(1):179–195, 2004.
97. F.A. Frey, M. F. Coffin, P. J. Wallace, and D. Weis. Leg 183 synthesis: Kerguelen Plateau–Broken Ridge—a large igneous province. In F.A. Frey, M.F. Coffin, P.J. Wallace, and P. G. Quilty, editors, *Proceedings of the Ocean Drilling Program, Scientific Results*, volume 183, pages 1–48, 2003.
98. S. Ingle, D. Weis, J. S. Scoates, and F. A. Frey. Relationship between the early Kerguelen plume and continental flood basalts of the paleo-Eastern Gondwanan margins. *Earth and Planetary Science Letters*, 197(1):35–50, 2002.
99. B. Kieffer, N. T. Arndt, and D. Weis. A bimodal alkalic shield volcano on Skiff Bank: its place in the evolution of the Kerguelen Plateau. *Journal of Petrology*, 43(7):1259–1286, 2002.
100. D. Weis and F. A. Frey. Submarine basalts of the Northern Kerguelen Plateau: Interaction between the Kerguelen plume and the Southeast Indian Ridge revealed at ODP Site 1140. *Journal of Petrology*, 43(7):1287–1309, 2002.
101. F. A. Frey, D. Weis, A. Y. Borisova, and G. Xu. Involvement of continental crust in the formation of the Cretaceous Kerguelen Plateau: New perspectives from ODP Leg 120 Sites. *Journal of Petrology*, 43(7):1207–1239, 2002.
102. J. J. Mahoney, W. B. Jones, F. A. Frey, V. J. M. Salters, D. G. Pyle, and H. L. Davies. Geochemical characteristics of lavas from Broken Ridge, the Naturaliste Plateau and southernmost Kerguelen Plateau: Cretaceous plateau volcanism in the southeast Indian Ocean. *Chemical Geology*, 120(3):315–345, 1995.
103. T. Gernon. Data associated with the paper "Enriched mantle generated through persistent convective erosion of continental roots". https://doi.org/10.6084/m9.figshare.30086716, 2025.

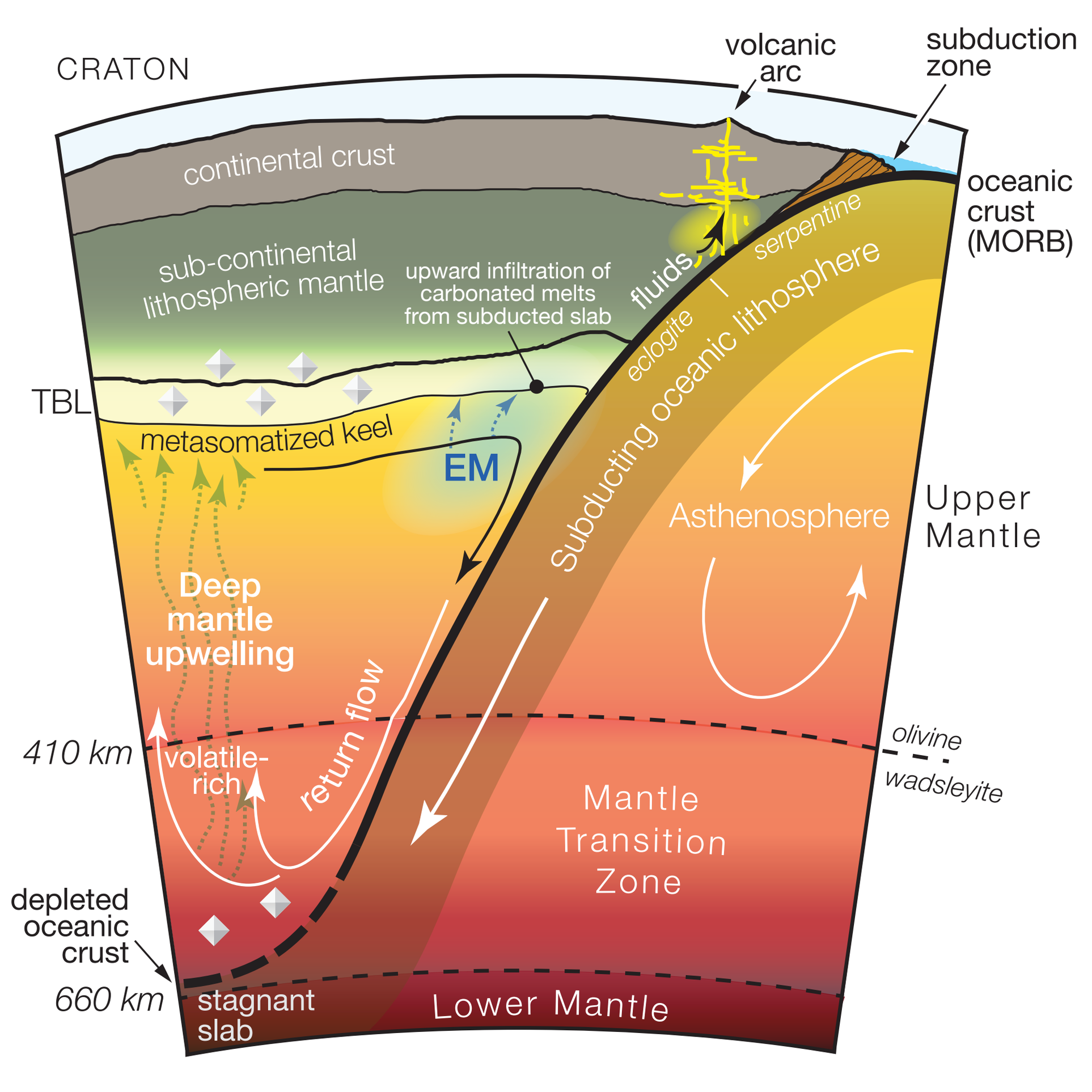
CRATON
volcanic arc
subduction zone
continental crust
oceanic crust (MORB)
sub-continental lithospheric mantle
upward infiltration of carbonated melts from subducted slab
fluids
serpentine
eclogite
Subducting oceanic lithosphere
TBL
metasomatized keel
EM
Asthenosphere
Upper Mantle
Deep mantle upwelling
return flow
410 km
volatile-rich
olivine
wadsleyite
Mantle Transition Zone
depleted oceanic crust
660 km
stagnant slab
Lower Mantle

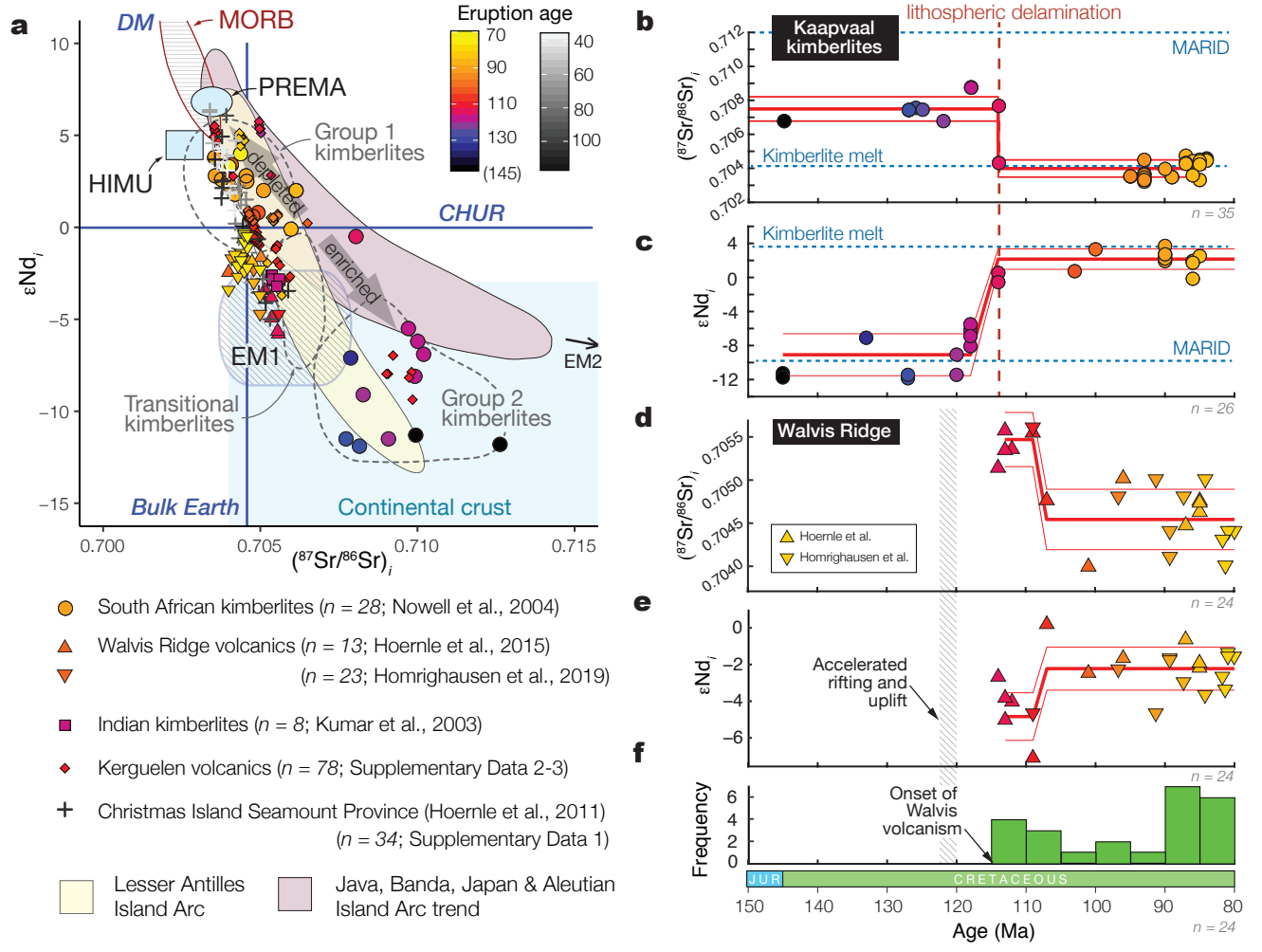
a
DM
MORB
PREMA
HIMU
Group 1 kimberlites
depleted
enriched
CHUR
EM1
EM2
Transitional kimberlites
Group 2 kimberlites
Bulk Earth
Continental crust
Eruption age
70
90
110
130
(145)
40
60
80
100
εNd$_i$
(87Sr/86Sr)$_i$
10
5
0
−5
−10
−15
0.700
0.705
0.710
0.715
South African kimberlites (n = 28; Nowell et al., 2004)
Walvis Ridge volcanics (n = 13; Hoernle et al., 2015)
(n = 23; Homrighausen et al., 2019)
Indian kimberlites (n = 8; Kumar et al., 2003)
Kerguelen volcanics (n = 78; Supplementary Data 2-3)
Christmas Island Seamount Province (Hoernle et al., 2011)
(n = 34; Supplementary Data 1)
Lesser Antilles Island Arc
Java, Banda, Japan & Aleutian Island Arc trend
b
Kaapvaal kimberlites
lithospheric delamination
MARID
Kimberlite melt
(87Sr/86Sr)$_i$
0.712
0.710
0.708
0.706
0.704
0.702
n = 35
c
Kimberlite melt
MARID
εNd$_i$
4
0
-4
-8
-12
n = 26
d
Walvis Ridge
Hoernle et al.
Homrighausen et al.
(87Sr/86Sr)$_i$
0.7055
0.7050
0.7045
0.7040
n = 24
e
εNd$_i$
0
−2
−4
−6
Accelerated rifting and uplift
n = 24
f
Frequency
6
4
2
0
Onset of Walvis volcanism
JUR
CRETACEOUS
150
140
130
120
110
100
90
80
Age (Ma)
n = 24

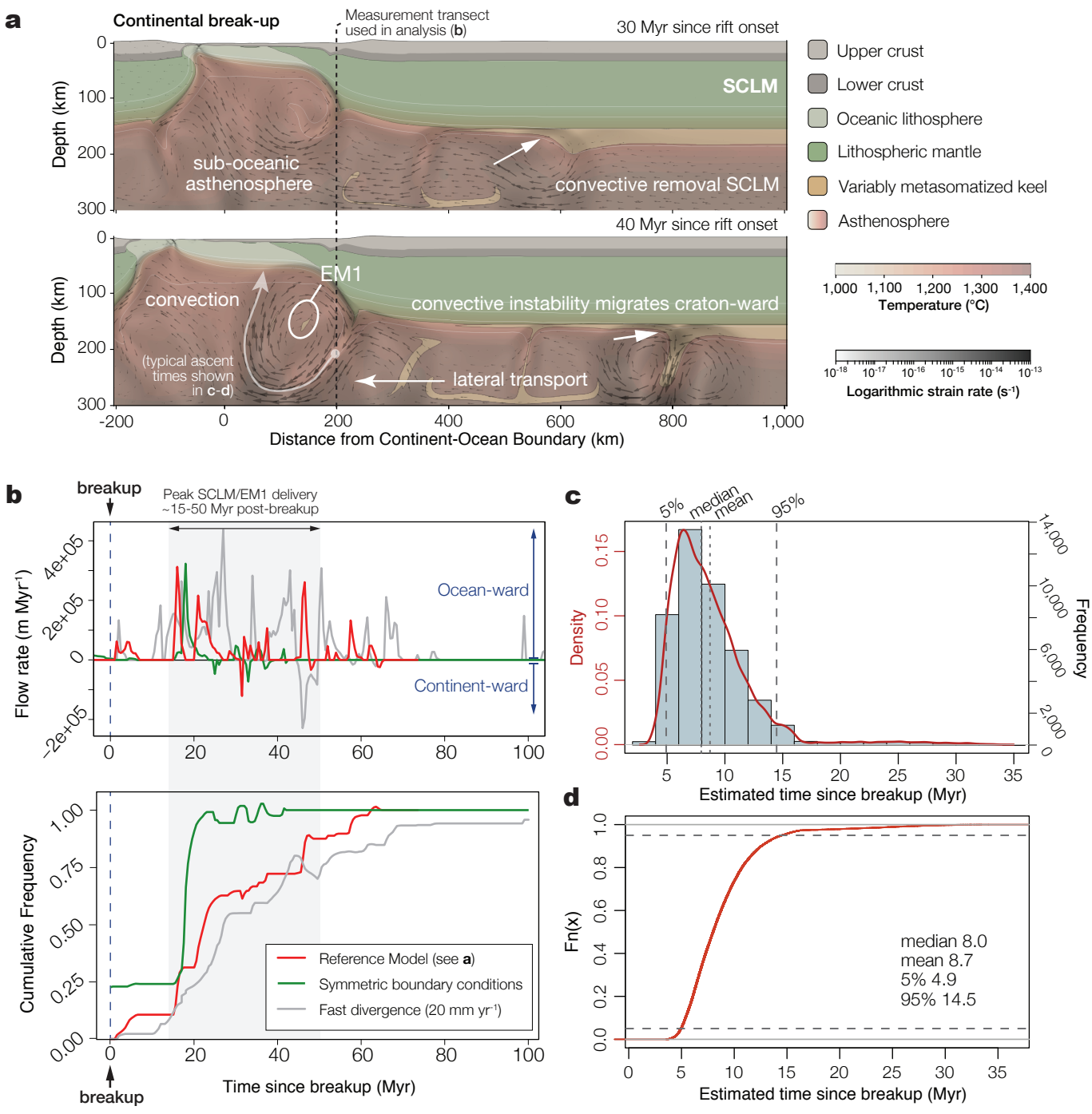
a
Continental break-up
Measurement transect used in analysis (b)
30 Myr since rift onset
SCLM
sub-oceanic asthenosphere
convective removal SCLM
40 Myr since rift onset
EM1
convection
convective instability migrates craton-ward
(typical ascent times shown in c-d)
lateral transport
Depth (km)
Distance from Continent-Ocean Boundary (km)
Upper crust
Lower crust
Oceanic lithosphere
Lithospheric mantle
Variably metasomatized keel
Asthenosphere
Temperature (°C)
Logarithmic strain rate (s-1)
b
breakup
Peak SCLM/EM1 delivery ~15-50 Myr post-breakup
Ocean-ward
Continent-ward
Flow rate (m Myr-1)
Cumulative Frequency
Reference Model (see a)
Symmetric boundary conditions
Fast divergence (20 mm yr-1)
Time since breakup (Myr)
c
5%
median
mean
95%
Density
Frequency
Estimated time since breakup (Myr)
d
Fn(x)
median 8.0
mean 8.7
5% 4.9
95% 14.5
Estimated time since breakup (Myr)

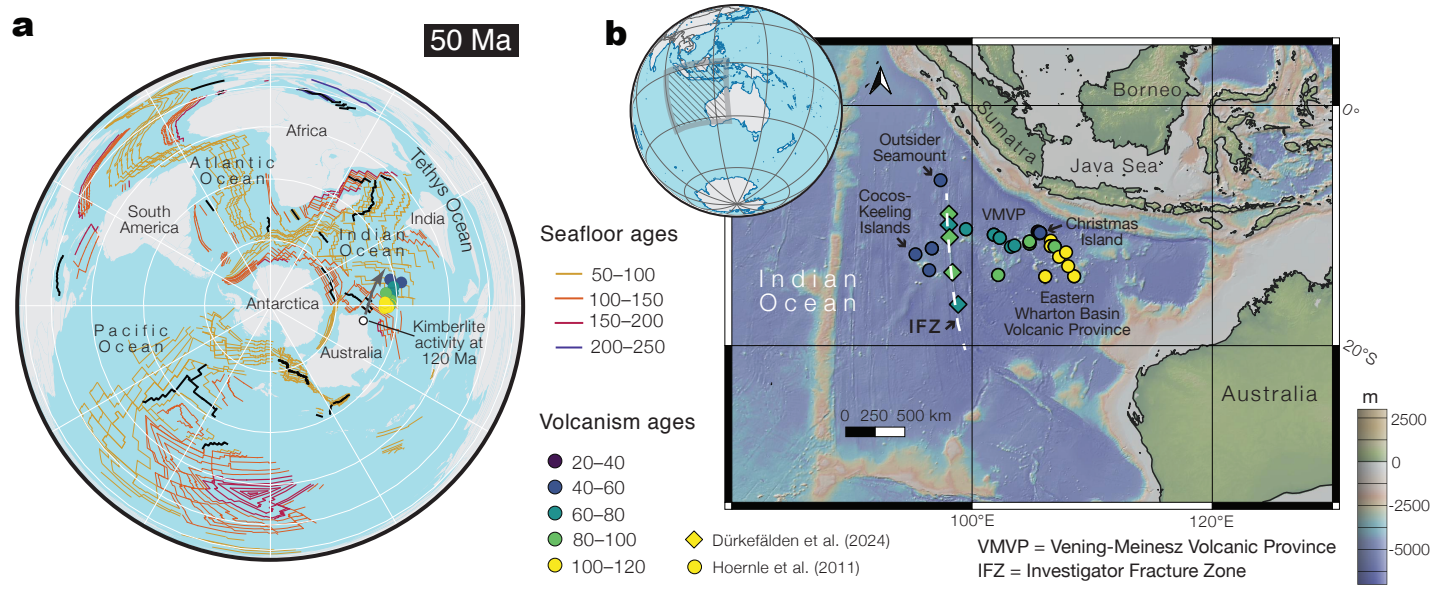
a
50 Ma
Africa
Atlantic Ocean
South America
Indian Ocean
India
Tethys Ocean
Antarctica
Pacific Ocean
Australia
Kimberlite activity at 120 Ma
b
Seafloor ages
50–100
100–150
150–200
200–250
Volcanism ages
20–40
40–60
60–80
80–100
100–120
Dürkefälden et al. (2024)
Hoernle et al. (2011)
Borneo
Sumatra
Java Sea
Outsider Seamount
Cocos-Keeling Islands
VMVP
Christmas Island
Indian Ocean
IFZ
Eastern Wharton Basin Volcanic Province
Australia
0 250 500 km
0°
20°S
100°E
120°E
m
2500
0
-2500
-5000
VMVP = Vening-Meinesz Volcanic Province
IFZ = Investigator Fracture Zone

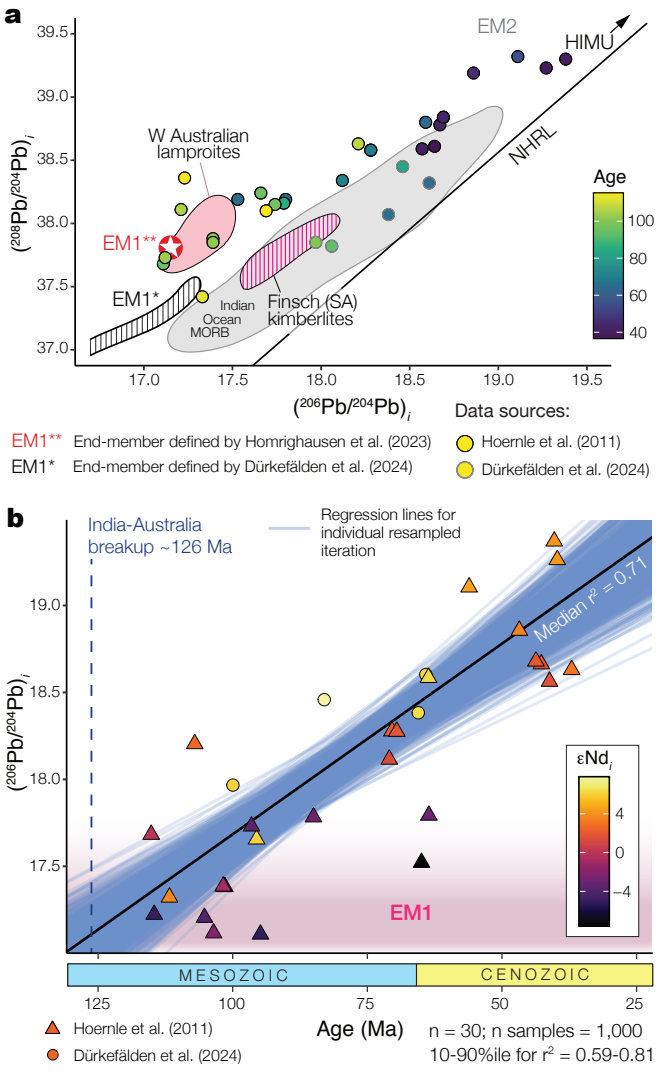
a
EM2
HIMU
NHRL
W Australian lamproites
EM1**
EM1*
Indian Ocean MORB
Finsch (SA) kimberlites
Age
100
80
60
40
39.5
39.0
38.5
38.0
37.5
37.0
17.0
17.5
18.0
18.5
19.0
19.5
(208Pb/204Pb)i
(206Pb/204Pb)i
EM1** End-member defined by Homrighausen et al. (2023)
EM1* End-member defined by Dürkefälden et al. (2024)
Data sources:
Hoernle et al. (2011)
Dürkefälden et al. (2024)
b
India-Australia breakup ~126 Ma
Regression lines for individual resampled iteration
Median r2 = 0.71
εNdi
4
0
−4
EM1
19.0
18.5
18.0
17.5
(206Pb/204Pb)i
MESOZOIC
CENOZOIC
125
100
75
50
25
Age (Ma)
Hoernle et al. (2011)
Dürkefälden et al. (2024)
n = 30; n samples = 1,000
10-90%ile for r2 = 0.59-0.81